Changes in the electronic structure of $BaTiO_3$ due to ferroelectric phase transition via polarization-dependent hard x-ray photoemission spectroscopy

Takeo Ohsawa
Research Center for Electronic and Optical Materials, National Institute for Materials Science, 1-1 Namiki, Tsukuba 305-0044, Japan

Shigenori Ueda
Research Center for Electronic and Optical Materials, National Institute for Materials Science, 1-1 Namiki, Tsukuba 305-0044, Japan
and
Synchrotron X-ray Station at SPring-8, National Institute for Materials Science, 1-1 Kouto, Sayo, Hyogo 679-5148, Japan

Takao Shimizu
Research Center for Electronic and Optical Materials, National Institute for Materials Science, 1-1 Namiki, Tsukuba 305-0044, Japan

Naoki Ohashi
Research Center for Electronic and Optical Materials, National Institute for Materials Science, 1-1 Namiki, Tsukuba 305-0044, Japan
and
Materials Research Center for Element Strategy, Tokyo Institute of Technology, Yokohama 226-8503, Japan

(Dated: April 3, 2025)

This study explored the changes in the electronic structure due to ferroelectric phase transition behavior of $BaTiO_3$. The temperature variations in the electronic structure of a ferroelectric $BaTiO_3$ crystal were investigated via hard X-ray photoemission spectroscopy (HAXPES) using linearly polarized X-rays and density functional theory calculations. The observed valence band HAXPES spectra exhibited distinct temperature-dependent shapes owing to the crystalline phase transitions from a high-temperature paraelectric cubic phase to low-temperature ferroelectric phases with tetragonal, orthorhombic, and rhombohedral symmetries. The changes in the valence band spectra agreed with the simulated HAXPES spectra derived from the projected densities of states in the crystalline phases multiplied by the photoionization cross-sections. This result suggests that the ferroelectric mechanism in $BaTiO_3$ is of the displacive type, which involves structural phase transformations.

I. INTRODUCTION

Ferroelectric materials are attractive for a broad range of applications such as actuators, capacitors, and memory devices [1–8]. These materials exhibit a switchable macroscopic polarization. One of the most technologically important ferroelectric oxides is the perovskite-type $BaTiO_3$, and the origin of its ferroelectric properties has long been controversial [9–11]. $BaTiO_3$, which has been extensively studied, exhibits rhombohedral (Rhom.), orthorhombic (Orth.), tetragonal (Tet.), and cubic (Cub.) phases. However, the microscopic nature of the phases and transitions in $BaTiO_3$ remains uncertain. In the popular displacive model [9, 10], the equilibrium position of each Ti atom is at the center of the oxygen octahedron in the Cub. phase. However, the Ti atoms are microscopically displaced along the <111>, <011>, and <001> directions in the Rhom., Orth., and Tet. phases, respectively. These displacements are regarded as the origin of ferroelectricity. Displacive-type transitions, which are assumed to occur in $BaTiO_3$, are described by the condensation of a soft phonon mode [10, 12]. This mode was observed in the Cub. phase via inelastic neutron scattering [13]. On the other hand, an order–disorder model, which was proposed to explain the phase transition behavior of $BaTiO_3$, has been supported by several experiments [14–16] and theoretical considerations [17, 18]. In this model, all Ti atoms are located in one of eight equivalent off-center positions, which are considered as potential minima along the <111> directions, for all crystalline phases [19]. In particular, the Ti atoms distort in the same direction in the low-temperature Rhom.

phase. Further investigation of the electronic structures of $BaTiO_3$ with different crystalline symmetries is needed to better understand its ferroelectric transitions, and one technical approach consists of using X-ray probes [20–23].

X-ray photoemission spectroscopy is a useful technique for studying electronic band structures in solids. In particular, hard X-ray photoemission spectroscopy (HAXPES) enables bulk-sensitive measurements of solid-state materials [24–26]. Owing to the relatively high kinetic energy (E_k of ∼4 keV or higher) of photoelectrons, resulting in a large inelastic mean free path (IMFP), HAXPES enables to probe the bulk electronic structures of solids, where the estimated information depth, IMFP × 3, is larger than 20 nm. Using linear dichroism in valence band (VB) HAXPES, electron orbitals can be selectively characterized [27–31]. Because the photoionization cross-section (σ) depends on the orbital character of the electrons (s, p, d, or f), principal quantum number, atomic number, and photon energy [32, 33], the σ values are closely correlated with the profiles of the HAXPES spectra and reflect the nature of the chemical bonding characteristics. Furthermore, the σ values are affected by the experimental geometry and X-ray polarization [27, 29–31]. Consequently, the HAXPES spectra measured at various temperatures using two different linearly polarized X-rays, which achieve linear dichroism in HAXPES, contain considerable information on the electronic band structures in solids. Hence, the combination of density functional theory (DFT) calculations and HAXPES offers a promising approach to revealing the changes in the electronic structure of $BaTiO_3$ due to the structural phase transitions caused by either displacive or order-disorder characteristics.

Herein, we investigate the phase transition behavior of $BaTiO_3$ based on observed and simulated VB HAXPES spectra. Temperature-dependent HAXPES measurements with linear dichroism revealed that the ferroelectric phase transitions of $BaTiO_3$ are of the displacive type, which is attributed to the displacement of the B-site ions. These results are critical for understanding the properties of ferroelectric materials and for providing guidance for improving nanoelectronic devices.

II. METHODS

A. Experimental details

HAXPES measurements were performed on $BaTiO_3$ single crystals at the undulator beamline BL15XU [25] of SPring-8, Japan. The $BaTiO_3$ crystals were preliminarily annealed in a gas mixture of hydrogen and nitrogen at 1120 °C to enhance the electrical conductivity before the crystals were introduced into the HAXPES apparatus [34]. The resistivity and carrier density of the annealed $BaTiO_3$ crystal measured in this study are 10 Ω cm and 3×10^{16} cm^{-3}, respectively, at 300 K, indicating that the conductivity does not interfere with the HAXPES measurements. An excitation energy ($h\nu$) of 6 keV was employed. All measurements were performed in the near-normal-emission geometry, where the incidence angle of the X-rays and the take-off angle of the photoelectrons were set to 2° and 88°, respectively, relative to the $BaTiO_3$(001) surface. The IMFP of the 6 keV photoelectrons inside $BaTiO_3$ was calculated to be ∼8.4 nm using the TPP-2M equation [35], leading to an information depth of ∼25.2 nm in this work. The VB linear dichroism in HAXPES was achieved using horizontal linearly polarized X-rays [E(H)], with an electric field vector ($\vec{E}$) parallel to the photoelectron trajectory ($\vec{\nu_e}$) to an electron analyzer, and vertical linearly polarized X-rays [E(V)], with $\vec{E}$ perpendicular to $\vec{\nu_e}$. The degrees of linear polarization (P_L) for the E(H) and E(V) X-rays were ∼1.00 and ∼0.70, respectively. The details of the experimental setup have been reported previously [36]. A total energy resolution of approximately 150 meV, evaluated from the Fermi edge of a pure gold film, was employed for the HAXPES measurements. For both the E(H) and E(V) X-rays, we measured the VB spectra at 118–426 K to investigate the spectroscopic characteristics induced by the phase transitions. The spectra were obtained from a multidomain structure when the crystalline form was in the Orth. and Rhom. phases at low temperatures.

B. Theoretical calculation

The electronic structures of $BaTiO_3$ were calculated using a plane-wave-based pseudo-potential method implemented in the CASTEP code [37]. The norm-conserved pseudopotentials were adopted, and the exchange-correlation energy was calculated using the Perdew-Burke-Ernzerhof functional revised for solids, known as PBEsol [38]. The plane-wave cut-off energy was set to 1050 eV, and a Monkhorst-Pack grid was used [39]. Structural optimizations were performed using the Broyden-Fletcher-Goldfarb-Shanno scheme [40], and the convergence of the energy minimization and structural relaxation was judged using the following tolerances: the tolerance for electronic energy mineralization was set to 5.0×10^{-7} eV/atom, the energy tolerance for structural optimization to 5.0×10^{-6} eV/atom, the force tolerance to 0.01 eV/Å, the stress tolerance to 0.02 GPa, and the atomic displacement tolerance to 5.0×10^{-4} Å. To reproduce the changes in the electronic structure due to phase transition, the electronic structures of Cub., Tet., Orth., and Rhom. $BaTiO_3$ were calculated by applying the symmetry constraints Pm3m, P4mm, Amm2, and R3m, respectively. After structural optimizations, the electronic structures were calculated using the hybrid PBE0 functional [41, 42] to better reproduce the electronic structure characteristics, such as a bandgap energy

III. RESULTS AND DISCUSSION

A. Hard X-ray photoemission spectroscopy of $BaTiO_3$

First, we present the VB spectra of $BaTiO_3$ obtained at several sets of temperatures. The VB spectra obtained using E(H) and E(V) X-rays and normalized by the photon flux are compared in Fig. 1(a). The normalized spectra are referred to as E(H)-VB and E(V)-VB. Note that the E(V)-VB spectra, which were corrected to P_L of ∼1.0, are shown in the figure by considering the intensity ratio of E(H) and E(V) X-rays [29, 36]. Regardless of the temperature, the intensities of the E(H)-VB spectra are higher than those of the E(V)-VB spectra. This difference is attributed to the variations in the σ values of all electron orbitals of $BaTiO_3$, as summarized in Table S1 for hν = 6 keV [33, 43, 44], and involves orbital characteristics, because the σ values depend on hν, $\vec{E}$, $\vec{\nu_e}$, and the electron orbitals.

The temperature-dependent shapes of the E(H)-VB and E(V)-VB spectra are not clearly distinguishable even across the phase transitions (Rhom.–Orth.–Tet.–Cub. transitions). Figure 1(b) compares the E(H)-VB and E(V)-VB spectra normalized at a peak intensity around a binding energy (E_B) of 6 eV. At each temperature, the spectral shapes around E_B = 7.8 eV differ between the E(H)-VB and E(V)-VB spectra. This discrepancy can be attributed to variations in the polarization-dependent σ values of the Ti 4s orbital (Table S1), as mentioned later. Except for this discrepancy, significant differences are not observed between the E(H)-VB and E(V)-VB spectra.

The temperature dependence of the E(H)-VB and E(V)-VB spectra was carefully analyzed. Figures 2(a) and (b) show the temperature dependences of the E(H)-VB and E(V)-VB spectra, respectively. The colors correspond to the crystalline phases shown in Fig. 1. The spectral shapes at each temperature are similar for the E(H)-VB and E(V)-VB spectra. Moreover, the spectral weight shifts monotonically to the lower E_B side as the temperature increases. This shift is more pronounced around the top of VB than at its bottom. Figures 2(c) and (d) show zoomed-in views of Figs. 2(a) and (b), respectively, in the vicinity of the top of VB. The temperature-dependent spectra can be categorized into four groups according to the phases: Rhom. (blue), Orth. (green), Tet. (orange), and Cub. (red). The temperature-dependent changes in the spectral shapes observed at $E_B \approx 4$ eV are also evident in the energy range around $E_B \approx 5.5$ eV. In contrast, the shoulder at the bottom of VB shows a narrowing spectral width; however, this change is less pronounced than the shifts observed around $E_B \approx 4$ eV and 5.5 eV. The spectral weight apparently shifts to the higher E_B side with decreasing temperature, suggesting a narrowing of the band width with reduced crystalline symmetry. This finding indicates that the band width increases with temperature and corresponds to different crystal forms.

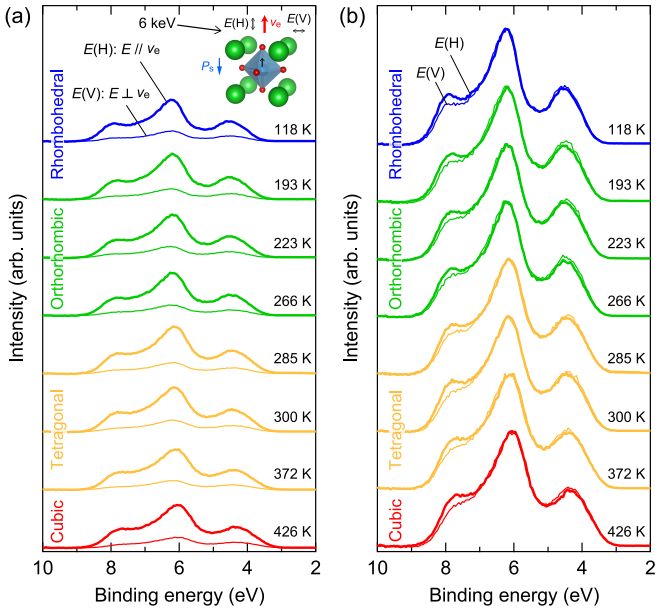

FIG. 1. (a) Valence band (VB) spectra of $BaTiO_3$ measured at several temperatures using 6 keV E(H) and E(V) X-rays. The colors correspond to the cubic (red), tetragonal (orange), orthorhombic (green), and rhombohedral (blue) crystalline phases. The inset shows the experimental geometry, where $\vec{\nu_e}$ and P_s indicate the photoelectron trajectory to the analyzer and the spontaneous polarization, respectively. (b) Normalized E(H)-VB and E(V)-VB spectra.

In this context, we discuss the location of the Fermi level (E_F). The behavior of the VB maximum (VBM) is shown in Figs. 2(c) and (d). Two possible explanations are considered: a shift in E_F with temperature and a change in the bandgap width with temperature. We investigated Ba 4d, Ti 2p, and O 1s core level spectra obtained using E(H) X-rays at various temperatures. These results reveal the E_B positions remain unchanged within each phase but exhibit very slight shifts across phase transitions. These slight shifts suggest changes in the chemical bonding states. Consequently we propose that the observed behavior is due to changes in the bandgap width rather than a shift in E_F, as DFT calculations indicate a systematic change in the bandgap width for different crystalline forms. In addition, because the crystal was heated in a hydrogen-containing gas stream at high temperature, the presence of significant charge carriers (electrons) at the bottom of the conduction band can be reasonably assumed. Actually, the VBM values shown in Fig. 2 are approximately 3.2–3.5 eV, which is consistent with the band gap values [45, 46]. Therefore, we assume that E_F remains very close to the bottom of the conduction band, regardless of the crystalline form.

These temperature-dependent spectral changes were not observed in n-type Nb:$SrTiO_3$(001) crystals with an electron density of $\sim 10^{20}$ cm^{-3}, even without annealing under the gas mixture (Fig. S1) because of the absence

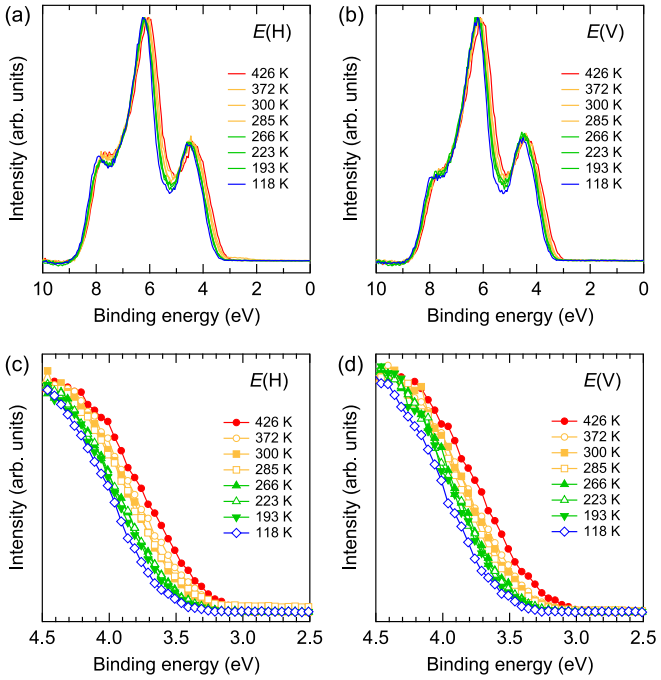

FIG. 2. Temperature dependence of the (a) E(H)-VB and (b) E(V)-VB spectra. Zoomed-in (c) E(H)-VB and (d) E(V)-VB spectra in the vicinity of the top of VB.

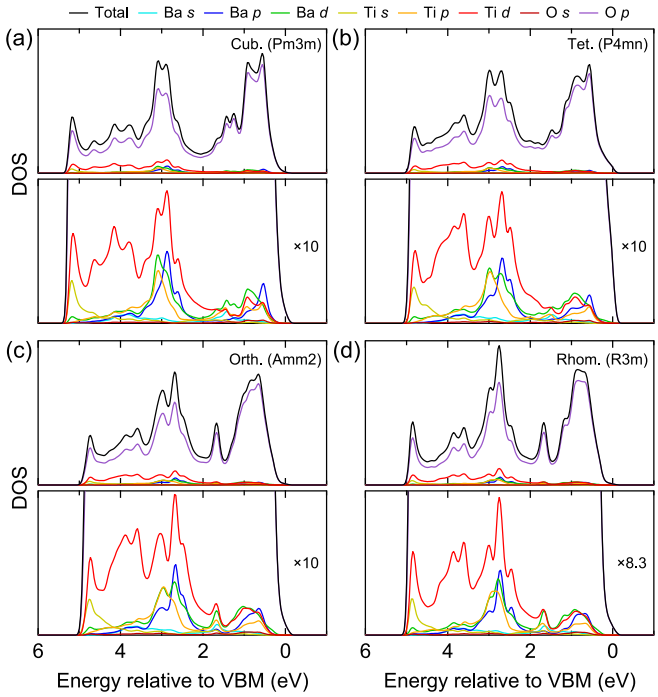

FIG. 3. Total and projected densities of states (DOSs) in the valence band region of $BaTiO_3$ for the (a) cubic (Cub.), (b) tetragonal (Tet.), (c) orthorhombic (Orth.), and (d) rhombohedral (Rhom.) phases. The upper and lower panels display the full and zoom-in scaled DOSs, respectively. The energy is referred to the valence band maximum (VBM).

of phase transitions in this temperature range. Additionally, Fig. S1 indicates that the peak broadening caused by thermal excitation does not account for the spectral changes observed in the E(H)-VB and E(V)-VB spectra of $BaTiO_3$, assuming similar magnitudes of thermal broadening for $SrTiO_3$ and $BaTiO_3$. Based on these results, we can assume that the spectral shifts near the top of VB and the increases in the band width, which are present in the E(H)-VB and E(V)-VB spectra, are associated with ferroelectric phase transitions.

B. Density functional theory calculations

All structural optimization calculations successfully satisfied the convergence tolerances. The crystal structures optimized using the PBEsol functional are provided as supplemental information in the CIF format, including R3m.cif, Amm2.cif, P4mm.cif, and Pm3m.cif. The electronic structures described below were calculated based on these optimized structures. Figure 3 shows the total and projected densities of states (PDOSs) for (a) Cub., (b) Tet., (c) Orth., and (d) Rhom. $BaTiO_3$ crystals obtained from DFT calculations using the PBE0 functional. As shown in the upper panels of Fig. 3, the VB is dominated by O $2p$ states, regardless of the crystalline form. In addition to the O $2p$ band, the Ti $3d$, $4s$, $4p$ and Ba $5p$, $5d$ bands contribute to the VB, as seen in the lower panels. Notably, the calculated energy bandgap decreases from that of Rhom. (4.20 eV) to that of Cub. (3.75 eV), as shown in Fig. S2. From Figs. 2 and 3, it is observed that the bandwidth increases, while the bandgap energy decreases with increasing temperature.

C. Simulated HAXPES

Using the PDOSs (Fig. 3) and σ values (Table S1), we simulated the HAXPES spectra [36]. The simulated HAXPES spectra were obtained by summing the PDOSs weighted with the σ values based on our experimental configuration. Figures 4(a) and (b) compare the simulated E(H)-VB and E(V)-VB spectra (upper plot) to the experimental spectra (lower plot). The energy was aligned to the bottom of VB at 6.0 eV in both the simulated and experimental spectra for comparison.

The shapes of the total DOSs and simulated spectra are not very similar. This is due to the variation in the σ values with respect to the elements and orbitals. According to Table S1 and Fig. 3, it is evident that the Ba $5p$ band is dominant in the simulated E(H)-VB and E(V)-VB spectra, as shown in Fig. S3. Although the VB is dominated by O $2p$ in terms of PDOS, the σ values for O $2p$ are very small under the experimental conditions employed in this study. As the σ value for Ti $4s$ is large in the E(H) configuration, the simulated E(H)-VB spectra represent the energy dispersion of Ba $5d$ (E_B ~3 eV)

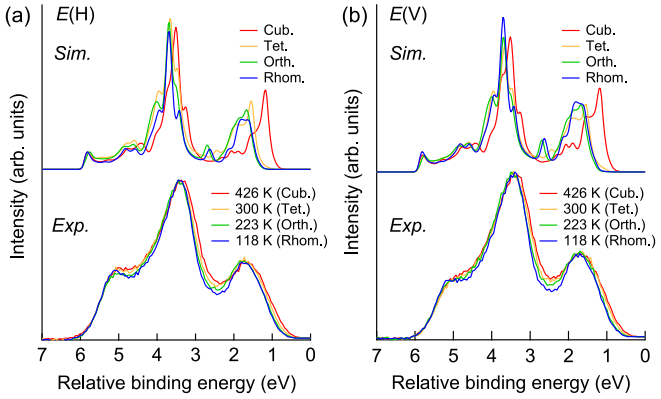

FIG. 4. Simulated (upper) and experimental (lower) VB spectra for (a) E(H) and (b) E(V) X-rays. The energy is aligned to the bottom of VB at 6.0 eV.

and Ti 4s (E_{B} ∼5 eV). Moreover, the Ba 5p, Ba 5d, and O 2p orbitals are relatively strong contributors to the simulated E(V)-VB spectra, where the Ti 4s band is suppressed owing to its small σ value in the E(V) configuration. As shown in Fig. 2, the band widths in both the E(H)-VB and E(V)-VB spectra increase with increasing temperature. This is consistent with the simulated spectra.

Here, the variation in the VB width is attributed to changes in the local structure, including the bond distance and angles. In the Cub. phase, the O–Ti–O angles are 180°, whereas in the other phases, these angles deviate from 180° owing to the structural distortion of the TiO_6 octahedron. Indeed, in the Rhom. phase, the angle is 173.15°, and in the Orth. phase, it ranges from 171.33° to 178.48°. In addition, for distorted TiO_6 coordination, the Ti–O distances vary in the ranges 1.887–2.111 Å in the Rhom. phase, 1.984–2.141 Å in the Orth. phase, and 1.848–2.189 Å in the Tet. phase. Regarding the coordination structure around Ba, the Ba–O distance in the Cub. phase is 2.81 Å, and it varies from 2.769 to 2.883 Å in the Rhom. phase, from 2.785 to 2.917 Å in the Orth. phase, and from 2.782 to 2.875 Å in the Tet. phase. Such distortions in the TiO_6 octahedron and BaO_{12} polyhedron can lead to the formation of a discrete electronic structure, resulting in a band structure with a small dispersion in the k-space. As shown in Figs. 2(c) and (d), the profiles of the HAXPES spectra can be classified into four groups according to their crystalline symmetry, and the variation in the spectral shapes does not change monotonically with temperature. Hence, the most important parameter for describing the electronic structures in $BaTiO_3$ should be the crystalline symmetry.

As mentioned in subsection III.A, spectral features depending on the crystalline symmetry were observed at $E_{\mathrm{B}} \approx 4$ and 5.5 eV in Fig. 2, manifesting as the narrowing of the major peaks in the E(H)-VB and E(V)-VB spectra. These features were well reproduced in the simulated E(H)-VB and E(V)-VB spectra. For example, the simulated spectra of the Cub. (red) and Tet. (orange) phases showed an extended tail around the VBM as well as in the range of approximately 2 eV on the energy scale, as shown in Fig. 4. The changes in the experimental VB width along the phase transition sequence agree with those in the DFT calculations.

In other words, the electronic structures probed using hard-X-ray photoemission technique indicated that the changes in the crystal structure accompanying the phase transition were reasonable.

A previous study indicated that the electronic structure of the Ti 3d orbital in Cub. $BaTiO_3$ is different from those in the other polar phases, as evidenced by X-ray absorption and fluorescence measurements [23]. Because the HAXPES spectra obtained in this study probe the electron orbital of Ba in $BaTiO_3$, the VB shift and changes in the band width provide evidence that the local structure and distortion of the BaO_{12} polyhedron responds to the phase-transition sequence. Although the Ba–O bond is nearly purely ionic, the electronic structure of the BaO_{12} polyhedron is strongly influenced by changes in the crystalline symmetry. Because the oxide ions in the BaO_{12} polyhedron are completely shared with the TiO_6 octahedron, the present results indicate that the electronic structure of the Ti–O bond is strongly affected by phase transition. Therefore, since such local distortion has been known as the displacive-type for the origin of ferroelectricity, we can conclude that the displacive model is more consistent in describing phase transitions in $BaTiO_3$ than the order-disorder model.

IV. CONCLUSIONS

Spectroscopic investigations of the phase transition behavior of $BaTiO_3$ were performed using linear polarization-dependent HAXPES measurements and DFT calculations. The combination of these methods showed that the variation in the spectroscopic profiles with temperature occurs stepwise rather than monotonically. The spectral features can be classified according to the Rhom., Orth., Tet., and Cub. crystalline phases of $BaTiO_3$. The simulated VB spectra derived from the PDOS and σ values agreed with the observed E(H)-VB and E(V)-VB spectra. This agreement suggests that the ferroelectric transition in $BaTiO_3$ is of the displacive type, which involves structural phase transformations. The measurements and analyses performed in this study, characterized by the large probing depth of HAXPES, provide detailed insights into the bulk electronic states of ferroelectric materials and emergent semiconductors. This technique constitutes a powerful diagnostic method for determining the band-selective electronic states of solids.

ACKNOWLEDGMENTS

The authors thank the staff of HiSOR, Hiroshima University, and JAEA/SPring-8 for the development of HXPES at BL15XU of SPring-8. The HXPES experiments were performed with the approval of the NIMS Synchrotron X-ray Station (Proposals Nos. 2014B4604, 2015A4603, 2015B4604, 2016B4603, 2019A4602, and 2019B4603). This work was also supported by MEXT Program: Data Creation and Utilization Type Material Research and Development Project Grant Number JPMXP1122683430. S.U. and N.O. acknowledge support from the Tokodai Institute for Elemental Strategy (TIES: Grant No. JPMXP0112101001) funded by the Ministry of Education, Culture, Sports, Science and Technology (MEXT), Japan.

AUTHOR CONTRIBUTIONS

T.O., S.U., and N.O. designed research; T.O., S.U., and N.O. performed the experiments; All authors discussed the results and wrote the paper.

[1] Z.-G. Ye, *Handbook of Advanced Dielectric, Piezoelectric and Ferroelectric Materials* (Woodhead Publishing, 2008).

[2] J. F. Scott and C. A. Paz de Araujo, Ferroelectric Memories, Science **246**, 1400 (1989).

[3] S.-E. Park and T. R. Shrout, Ultrahigh strain and piezoelectric behavior in relaxor based ferroelectric single crystals, Journal of Applied Physics **82**, 1804 (1997).

[4] L. E. Cross, Relaxor ferroelectrics, Ferroelectrics **76**, 241 (1987).

[5] G. H. Haertling, Ferroelectric Ceramics: History and Technology, in *Ferroelectricity*, Vol. 818 (Wiley-VCH Verlag GmbH, Weinheim, Germany, 2007) pp. 157–178.

[6] J. F. Scott, Applications of Modern Ferroelectrics, Science **315**, 954 (2007).

[7] M. Dawber, K. M. Rabe, and J. F. Scott, Physics of thin-film ferroelectric oxides, Reviews of Modern Physics **77**, 1083 (2005).

[8] D. Damjanovic, Ferroelectric, dielectric and piezoelectric properties of ferroelectric thin films and ceramics, Reports on Progress in Physics **61**, 1267 (1998).

[9] W. Cochran, Crystal Stability and the Theory of Ferroelectricity, Physical Review Letters **3**, 412 (1959).

[10] W. Cochran, Crystal stability and the theory of ferroelectricity, Advances in Physics **9**, 387 (1960).

[11] R. E. Cohen, Origin of ferroelectricity in perovskite oxides, Nature **358**, 136 (1992).

[12] J. C. Slater, The lorentz correction in barium titanate, Physical Review **78**, 748 (1950).

[13] J. Harada, J. D. Axe, and G. Shirane, Neutron-scattering study of soft modes in cubic $BaTiO_3$, Physical Review B **4**, 155 (1971).

[14] I. Bersuker, On the origin of ferroelectricity in perovskite-type crystals, Physics Letters **20**, 589 (1966).

[15] R. Comes, M. Lambert, and A. Guinier, The chain structure of $BaTiO_3$ and $KNbO_3$, Solid State Communications **6**, 715 (1968).

[16] K. Tsuda, R. Sano, and M. Tanaka, Nanoscale local structures of rhombohedral symmetry in the orthorhombic and tetragonal phases of $BaTiO_3$ studied by convergent-beam electron diffraction, Physical Review B **86**, 214106 (2012).

[17] H. Takahasi, A Note on the Theory of Barium Titanate, Journal of the Physical Society of Japan **16**, 1685 (1961).

[18] M. Stachiotti, A. Dobry, R. Migoni, and A. Bussmann-Holder, Crossover from a displacive to an order-disorder transition in the nonlinear-polarizability model, Physical Review B **47**, 2473 (1993).

[19] A. S. Chaves, F. C. S. Barreto, R. A. Nogueira, and B. Zẽks, Thermodynamics of an eight-site order-disorder model for ferroelectrics, Physical Review B **13**, 207 (1976).

[20] B. Ravel, E. A. Stern, R. I. Vedrinskii, and V. Kraizman, Local structure and the phase transitions of $BaTiO_3$, Ferroelectrics **206-207**, 407 (1998).

[21] Y. Isohama, N. Nakajima, H. Maruyama, Y. Tezuka, and T. Iwazumi, Tetragonal-cubic phase transition in $BaTiO_3$ probed by resonant X-ray emission spectroscopy, Journal of Electron Spectroscopy and Related Phenomena **184**, 207 (2011).

[22] A. Pancotti, J. Wang, P. Chen, L. Tortech, C.-M. Teodorescu, E. Frantzeskakis, and N. Barrett, X-ray photoelectron diffraction study of relaxation and rumpling of ferroelectric domains in $BaTiO_3(001)$, Physical Review B **87**, 184116 (2013).

[23] Y. Tezuka, S. Nozawa, N. Nakajima, and T. Iwazumi, Temperature dependence of electronic structure on the ferroelectric phase transition of $BaTiO_3$, Physical Review B **104**, 235148 (2021).

[24] K. Kobayashi, Hard X-ray photoemission spectroscopy, Nuclear Instruments and Methods in Physics Research, Section A: Accelerators, Spectrometers, Detectors and Associated Equipment **601**, 32 (2009).

[25] S. Ueda, Y. Katsuya, M. Tanaka, H. Yoshikawa, Y. Yamashita, S. Ishimaru, Y. Matsushita, K. Kobayashi, R. Garrett, I. Gentle, K. Nugent, and S. Wilkins, Present Status of the NIMS Contract Beamline BL15XU at SPring-8, in *AIP Conf. Proc.*, Vol. 1234 (2010) pp. 403–406.

[26] A. X. Gray, C. Papp, S. Ueda, B. Balke, Y. Yamashita, L. Plucinski, J. Minár, J. Braun, E. R. Ylvisaker, C. M. Schneider, W. E. Pickett, H. Ebert, K. Kobayashi, and C. S. Fadley, Probing bulk electronic structure with hard X-ray angle-resolved photoemission, Nature Materials **10**, 759 (2011).

[27] A. Sekiyama, J. Yamaguchi, A. Higashiya, M. Obara, H. Sugiyama, M. Y. Kimura, S. Suga, S. Imada, I. A. Nekrasov, M. Yabashi, K. Tamasaku, and T. Ishikawa, The prominent 5d-orbital contribution to the conduction electrons in gold, New Journal of Physics **12**, 043045 (2010).

[28] A. Sekiyama, A. Higashiya, and S. Imada, Polarization-

dependent hard X-ray photoemission spectroscopy of solids, Journal of Electron Spectroscopy and Related Phenomena **190**, 201 (2013).

[29] S. Ueda and I. Hamada, Polarization Dependent Bulk-sensitive Valence Band Photoemission Spectroscopy and Density Functional Theory Calculations: Part I. $3d$ Transition Metals, Journal of the Physical Society of Japan **86**, 124706 (2017).

[30] S. Ueda and I. Hamada, Polarization dependent bulk-sensitive valence band photoemission spectroscopy and density functional theory calculations: Part II. $4d$ transition metals, Journal of the Physical Society of Japan **90**, 1 (2021).

[31] S. Ueda and I. Hamada, Polarization-dependent Bulk-sensitive Valence Band Photoemission Spectroscopy and Density Functional Theory Calculations: Part III. $5d$ Transition Metals, Journal of the Physical Society of Japan **91**, 1 (2022).

[32] J. Yeh and I. Lindau, Atomic subshell photoionization cross sections and asymmetry parameters: $1 < Z < 103$, Atomic Data and Nuclear Data Tables **32**, 1 (1985).

[33] M. Trzhaskovskaya, V. Nikulin, V. Nefedov, and V. Yarzhemsky, Non-dipole second order parameters of the photoelectron angular distribution for elements Z=1–100 in the photoelectron energy range 1–10keV, Atomic Data and Nuclear Data Tables **92**, 245 (2006).

[34] T. Ohsawa, S. Hirose, and N. Ohashi, Potential barrier formed at domain boundaries in twinned tetragonal $BaTiO_3$ single crystals, Applied Physics Letters **110**, 011604 (2017).

[35] S. Tanuma, C. J. Powell, and D. R. Penn, Calculations of electron inelastic mean free paths. V. Data for 14 organic compounds over the 50–2000 eV range, Surface and Interface Analysis **21**, 165 (1994).

[36] T. Ohsawa, S. Ueda, M. Suzuki, Y. Tateyama, J. R. Williams, and N. Ohashi, Investigating crystalline-polarity-dependent electronic structures of GaN by hard x-ray photoemission and ab-initio calculations, Applied Physics Letters **107**, 171604 (2015).

[37] S. J. Clark, M. D. Segall, C. J. Pickard, P. J. Hasnip, M. I. J. Probert, K. Refson, and M. C. Payne, First principles methods using CASTEP, Zeitschrift für Kristallographie - Crystalline Materials **220**, 567 (2005).

[38] J. P. Perdew, A. Ruzsinszky, G. I. Csonka, O. A. Vydrov, G. E. Scuseria, L. A. Constantin, X. Zhou, and K. Burke, Restoring the Density-Gradient Expansion for Exchange in Solids and Surfaces, Physical Review Letters **100**, 136406 (2008).

[39] J. D. Pack and H. J. Monkhorst, Special points for Brillouin-zone integrations, Physical Review B **16**, 1748 (1977).

[40] B. G. Pfrommer, M. Côté, S. G. Louie, and M. L. Cohen, Relaxation of Crystals with the Quasi-Newton Method, Journal of Computational Physics **131**, 233 (1997).

[41] J. P. Perdew, M. Ernzerhof, and K. Burke, Rationale for mixing exact exchange with density functional approximations, The Journal of Chemical Physics **105**, 9982 (1996).

[42] C. Adamo and V. Barone, Toward reliable density functional methods without adjustable parameters: The PBE0 model, The Journal of Chemical Physics **110**, 6158 (1999).

[43] M. Trzhaskovskaya, V. Nefdov, and V. Yarzhemsky, Photoelectron angular distribution parameters for elements Z=1 to Z=54 in the photoelectron energy range 100–5000 eV, Atomic Data and Nuclear Data Tables **77**, 97 (2001).

[44] J. Scofield, *Lawrence Livermore Laboratory; Tech. Rep. UCRL-; 51326*, Tech. Rep. (Divison of Technical Information Extension, U.S. Atomic Energy Commission, 1973).

[45] M. Cardona, Optical Properties and Band Structure of $SrTiO_3$ and $BaTiO_3$, Physical Review **140**, A651 (1965).

[46] J. Narvaez, F. Vasquez-Sancho, and G. Catalan, Enhanced flexoelectric-like response in oxide semiconductors, Nature **538**, 219 (2016).